Age and thermal history of the Geysers plutonic complex (felsite unit), Geysers geothermal field, California: a ^{40}Ar/^{39}Ar and U–Pb study

G. Brent Dalrymple [a],*, Marty Grove [b], Oscar M. Lovera [b], T. Mark Harrison [b], Jeffrey B. Hulen [c], Marvin A. Lanphere [d]

[a] *College of Oceanic and Atmospheric Sciences, Oregon State University, Corvallis, OR 97331, USA*
[b] *Department of Earth and Space Sciences, and Institute of Geophysics and Planetary Physics, University of California, Los Angeles, CA 90024, USA*
[c] *Energy and Geoscience Institute, University of Utah, Salt Lake City, UT 84108, USA*
[d] *U.S. Geological Survey, 345 Middlefield Road, Menlo Park, CA 94025, USA*

Abstract

Sixty-nine ion microprobe spot analyses of zircons from four granite samples from the plutonic complex that underlies the Geysers geothermal field yield ^{207}Pb/^{206}Pb vs. ^{238}U/^{206}Pb concordia ages ranging from 1.13 ± 0.04 Ma to 1.25 ± 0.04 (1σ) Ma. The weighted mean of the U/Pb model ages is 1.18 ± 0.03 Ma. The U–Pb ages coincide closely with ^{40}Ar/^{39}Ar age spectrum plateau and 'terminal' ages from coexisting K-feldspars and with the eruption ages of overlying volcanic rocks. The data indicate that the granite crystallized at 1.18 Ma and had cooled below 350ºC by ∼0.9–1.0 Ma. Interpretation of the feldspar ^{40}Ar/^{39}Ar age data using multi-diffusion domain theory indicates that post-emplacement rapid cooling was succeeded either by slower cooling from 350º to 300ºC between 1.0 and 0.4 Ma or transitory reheating to 300–350ºC at about 0.4–0.6 Ma. Subsequent rapid cooling to below 260ºC between 0.4 and 0.2 Ma is in agreement with previous proposals that vapor-dominated conditions were initiated within the hydrothermal system at this time. Heat flow calculations constrained with K-feldspar thermal histories and the present elevated regional heat flow anomaly demonstrate that appreciable heat input from sources external to the known Geysers plutonic complex is required to maintain the geothermal system. This requirement is satisfied by either a large, underlying, convecting magma chamber (now solidified) emplaced at 1.2 Ma or episodic intrusion of smaller bodies from 1.2 to 0.6 Ma. © 1999 Elsevier Science B.V. All rights reserved.

Keywords: The Geysers; geothermal fields; Ar-40/Ar-39; U/Pb; heat flows; anomalies; heating

1. Introduction

The Geysers steam field, in northwest central California (Fig. 1) is the world's largest known vapor-dominated geothermal system and yields about 1 GW of electrical energy [1]. The Geysers–Clear Lake thermal anomaly (Fig. 1) is spatially coincident with the Pliocene–Holocene Clear Lake volcanic field (CLVF). The CLVF is the youngest [2,3] in a series of volcanic centers developed along the North American–Pacific plate transform boundary [4]. The distribution of the present 600 km^2 Geysers steam field [5] correlates directly with the most intense

---

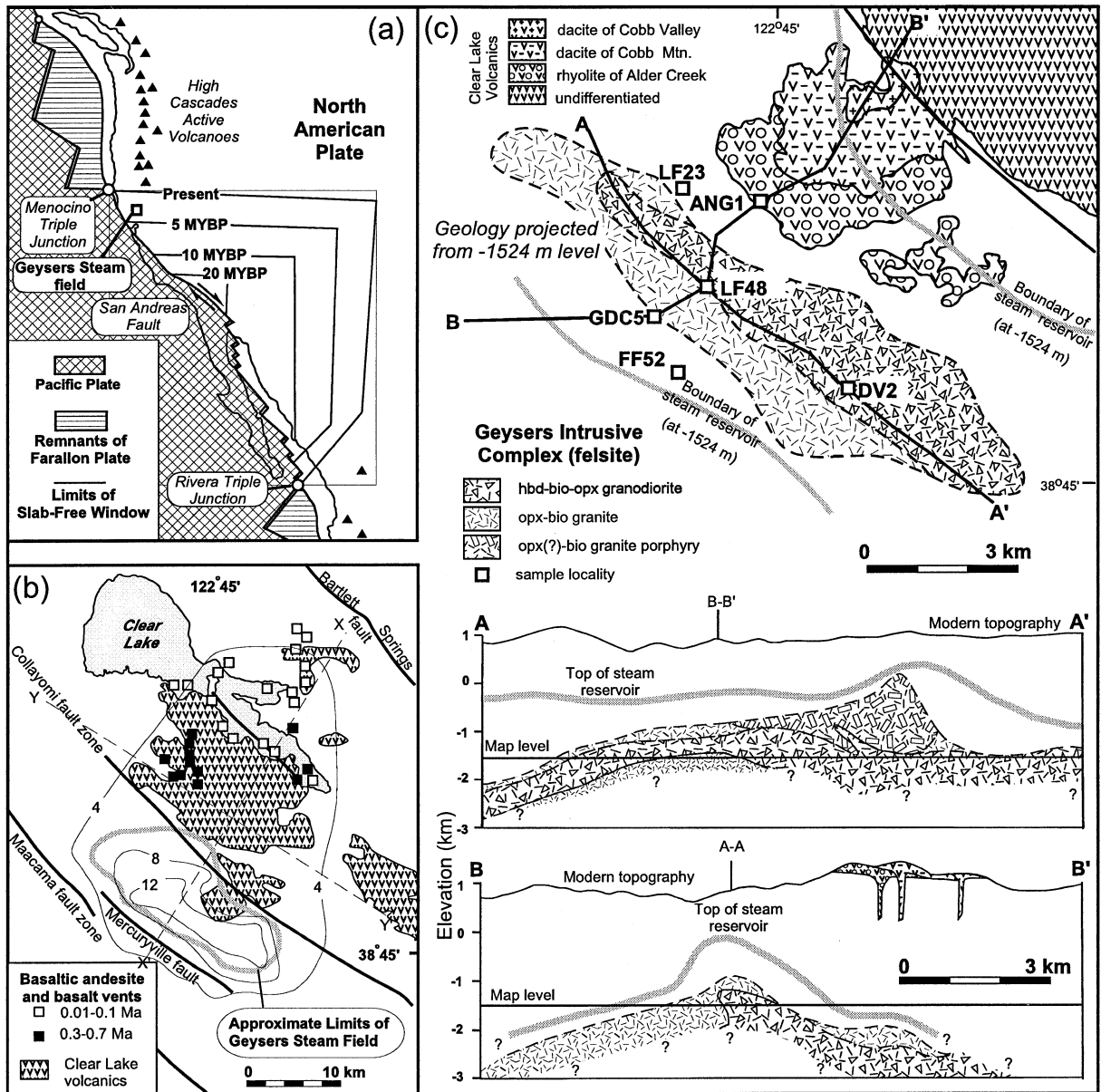* Corresponding author. Fax: +1 541 737 2064; E-mail: gbd@oce.orst.edu

Fig. 1. Location and tectonic setting of Geysers geothermal field. (a) Late Cenozoic tectonic evolution of western North America [20]. (b) Clear Lake volcanic field (CLVF) with surface heat flow contours in hfu [6,21]. Open and filled squares represent dated volcanic vents [2,3]. Surface heat flow profiles X–X'' and Y–Y'' are shown in Fig. 6a. (c) Map and cross sections show subsurface occurrence of Geysers plutonic complex (GPC) [9], well locations for analyzed samples (open squares), and volcanic rocks of the CLVF [3,11].

surface heat flow anomaly (about 500 mW/m²) in the CLVF [6]. The steam field is localized within and above a composite, >100 km³ Quaternary plutonic body ('the felsite') that consists of granite, microgranite porphyry, and granodiorite and occurs only in the subsurface [7–10]. The felsite (more accurately and henceforth called the Geysers plutonic complex or GPC) underlies equivalent (?) extrusive material of the CLVF that is collectively referred to as the Cobb Mountain volcanic center [3,11].

A fundamental unresolved issue regarding the Geysers steam field is the nature and location of its heat source(s). While it seems evident that thermal energy from cooling intrusions within the GPC triggered and maintained the precursor fluid-dominated system [1], the importance of residual magmatic heat from the GPC for maintaining the modern steam field is far less certain. Specifically, since the GPC is a shallow body that was apparently emplaced ~1 m.y. ago [7,8,12–14], it should have cooled by now to near ambient background temperatures [15].

Most earlier K–Ar and ^{40}Ar/^{39}Ar age studies were limited in scope and value. For example, the reported range of K–Ar and total fusion ^{40}Ar/^{39}Ar ages measured from materials from different locations within the GPC is 0.6–2.7 Ma [7,8,13]. Preliminary ^{40}Ar/^{39}Ar step-heating measurements of K-feldspars from granite and microgranite porphyry were interpreted as suggesting emplacement perhaps as early as 1.3–1.4 Ma [14]. Microgranite porphyry dikes sampled well above the GPC have yielded ^{40}Ar/^{39}Ar ages from 0.6 Ma (total fusion) [13] to 1.1 Ma (age spectrum) [12]. The difficulty in interpreting these results may be partly due to diffusive loss of radiogenic ^{40}Ar (^{40}Ar*) or uptake of excess ^{40}Ar* (^{40}Ar$_E$) in this environment as well as to the limited nature of the studies.

Recently, K-feldspar ^{40}Ar/^{39}Ar step-heating results from the granodiorite strongly indicate emplacement at 1.09 ± 0.02 Ma (1σ) [12]. These authors also produced the only detailed ^{40}Ar/^{39}Ar thermal history result from a sample of hydrothermally precipitated adularia from the northwestern part of the steam field. Their modeling indicates formation at 330ºC at 0.57 Ma followed by rapid cooling from >300ºC to <260ºC at ~0.25 Ma, marking the onset of steam-dominated conditions in the hydrothermal system.

To better understand the emplacement history and thermal evolution of the GPC, we have measured ion microprobe U–Pb zircon ages and performed K-feldspar ^{40}Ar/^{39}Ar thermal history analysis with a suite of drill hole samples from the granite. The new data confirm that sampled portions of the GPC are sufficiently old that its residual magmatic heat is inadequate to maintain the modern geothermal system. Elevated heat flow [6], Quaternary–Holocene volcanism [2], and geophysical imaging of the CLVF [16,17] have been interpreted to indicate that ei-

ther a large (~14 km diameter) magma chamber at ~7 km depth [16,18] or smaller, episodically intruded bodies [17] underlie the CLVF. To evaluate these possibilities we use K-feldspar ^{40}Ar/^{39}Ar thermal histories obtained with the multi-diffusion domain (MDD) approach [19] to constrain heat flow calculations that assess the possible nature (size, location, age) of additional intrusions.

2. Geologic setting

The CLVF [2,3] is the northernmost and youngest in a chain of volcanic fields that extend several hundred kilometers to the southeast along and within the eastern part of the San Andreas fault (SAF) transform system (Fig. 1). Northward propagation of the Mendocino triple junction has occurred over the past 30 m.y. as subduction of the Juan de Fuca plate beneath western North America was progressively supplanted by Pacific–North American plate interaction [20]. Development of volcanic fields in the Coast Ranges is believed by many to be linked to upwelling of asthenospheric mantle along the trailing edge of subducted and abandoned oceanic lithosphere thrust beneath North America [21–23]. Consensus among these workers is that the lithospheric 'gap' that forms between the newly initiated transform margin and the formerly subducting oceanic plate is relatively short-lived (<2–3 m.y.) at any one location. Its existence permits focused ascent and decompressional melting of asthenosphere, resulting in volcanic centers and coeval plutonic bodies such as the CLVF and GPC [24].

The GPC comprises three readily recognizable intrusive rock types [9]: biotite–orthopyroxene granite, biotite–pyroxene (?) microgranite porphyry, and hornblende–biotite–orthopyroxene granodiorite. The granite and the microgranite are compositional equivalents that differ principally in texture and occurrence: the former is fine-grained hypidiomorphic and occurs at the highest elevations in the complex (Fig. 1), while the latter is granophyric and occupies deeper regions. Based upon the petrographic data and the distribution of the lithologies in drill holes [9] it appears likely that the granite and microgranite are cogenetic and older than the granodiorite, which occurs mostly at depth along the northeastern portion of the intrusive complex. Comparison with

the overlying volcanic rocks [9,12] indicates that the granodiorite is likely the intrusive equivalent of the 1.1 Ma dacite [3], while the granite and microgranite are probably related to the 1.2 Ma rhyolite [11].

The Geysers steam field extends from deep within the GPC upwards into Franciscan metaclastic and metavolcanic host rocks [5]. Now vapor-dominated, it was once a high-temperature, hot-water system that precipitated hydrothermal mineral assemblages in zones symmetrical about the GPC. Stable isotopic and fluid inclusion data indicate that early-stage alteration involved magmatic brine. Throughout much of the field near-constant 35 bar, 240°C, low-salinity conditions indicate that steam is the pressure-controlling medium. However, the presence of high-Cl, high ^{3}He/^{4}He, δ^{18}O-enriched, high-temperature steam underlying the 'normal' reservoir in the northwestern field seems to indicate recent intrusion there [1].

Deformation, including development of northwest-trending wrench faults and ancillary extensional structures consistent with uniaxial extension [25], appears to have strongly influenced the distribution of both the GPC and the hydrothermal system. Elongate geometry and minimal assimilation of the Francis-can wall rocks [9] is consistent with emplacement of the GPC in a pull-apart basin [10]. The steam field's northeastern and southwestern margins coincide with the right-lateral Collayomi and Mercuryville faults (Fig. 1). The Bartlett Springs fault zone bounds most of the CLVF on the north, and a northeast-trending extensional belt linking that structure with the Maacama fault southwest of the Geysers is the locus of all deep, high-temperature (>300°C) exploration wells completed in the region [17].

3. Sampling and analytical methods

Feldspar, biotite, and zircon were concentrated from air drill cuttings using standard magnetic and density techniques. Our samples (Table 1; Fig. 1) represent 20-ft (∼7 m) intervals from drill holes penetrating the GPC. We have abbreviated the sample numbers. Characters to the left of the hyphen indicate the well while those to the right give the depth from the top of the well (in feet, consistent with industry practice) to the top of the sampling interval. Complete sample numbers, sample descriptions,

Table 1
Terminal and high-*T* plateau ages from ^{40}Ar/^{39}Ar age spectra on K-feldspar and biotite from the GPC, Geysers geothermal field

Sample No.	Unit [a]	Mineral [b]	Terminal age [b] (Ma ± 1σ)	No. of steps	^{39}Ar$_K$ (% of total)	E (kcal/mol)	$\log(D_0/r_0^2)$
ANG1-11400	g	Ksp (T)	1.18 ± 0.04	2	13.3	48.8 ± 2.0	6.1 ± 1.0
		Ksp	1.05 ± 0.02	3	5.1		
ANG1-11440	g	Ksp (T)	1.13 ± 0.08	2	9.7	49.2 ± 3.0	6.3 ± 1.2
		Ksp	1.22 ± 0.3	2	2.4		
DV2-3708	mg	Ksp	0.67 ± 0.01	9	61.9		
FF52-9040	g	Ksp (T)	1.20 ± 0.01	5	60.0	43.5 ± 0.9	3.7 ± 0.2
		Ksp	1.18 ± 0.01	3	20.4		
		bio	1.07 ± 0.02	4	28.2		
FF52-9140	g	Ksp	1.21 ± 0.07	1	7.6		
		bio	1.09 ± 0.03	5	47.7		
GDC5-7240	g	Ksp	0.91 ± 0.17	1	3.8		
		bio	0.93 ± 0.03	9	91.8		
GDC5-7800	g	Ksp (T)	0.87 ± 0.02	3	20.9	48.1 ± 2.5	5.5 ± 1.0
LF23-9540	g	Ksp	1.14 ± 0.01	9	66.3		
LF23-9800	g	Ksp (T)	0.94 ± 0.01	5	55.1	47.2 ± 1.5	5.2 ± 0.4
		Ksp	0.98 ± 0.02	9	44.0		
LF48-8089	mg	Ksp	0.99 ± 0.01	3	25.4		

[a] g = biotite–pyroxene granite; mg = biotite microgranite porphyry. [b] Ksp = K-feldspar; bio = biotite; (T) = analyzed at UCLA and used for thermal modeling. Other samples analyzed at USGS, Menlo Park. [c] Plateau age or terminal age indicated by a consistent group of high *T* steps. Sometimes the last few steps, which are typically small and fractionated, are omitted. Selection of terminal ages is subjective and may have minimal age significance. Weighted mean and error, σ_{best}, [41] of terminal or plateau steps.

and U–Pb and Ar analytical data can be obtained from the archived data at http://oro.ess.ucla.edu. All errors reported here are 1σ.

3.1. $^{40}Ar/^{39}Ar$

Initial Ar analyses were performed at the USGS in Menlo Park. Cadmium-shielded samples were irradiated for 2 h in the core of the USGS TRIGA reactor using sanidine from the Taylor Creek Rhyolite (85G003, 27.92 Ma) as a neutron fluence monitor [14,26]. Step heating involved a double-vacuum furnace while Ar analyses were performed with a MAP-216 mass spectrometer equipped with a Baur-Signer source and an electron multiplier. Temperature calibration and heating schedules were not designed to recover detailed thermal history information but the chronologic significance of the age spectra remains undiminished.

To produce data suitable for thermal history modeling, additional $^{40}Ar/^{39}Ar$ analyses were performed on five K-feldspars (Table 1) at UCLA using higher-resolution heating schedules. These samples were irradiated for 5 h unshielded in the L67 position of the Ford Reactor, University of Michigan, using Fish Canyon sanidine (27.8 Ma) as the neutron fluence monitor. Step heating employed a double-vacuum furnace with ±5ºC temperature control. Ar isotopic analyses were performed with a VG 3600 mass spectrometer [27]. Successive, low-temperature, isothermal heating steps were performed to evaluate the validity of the low-temperature Arrhenius data [28] and to generate data required to correct $^{40}Ar^*/^{39}Ar_K$ for Cl-correlated $^{40}Ar_E$ released by decrepitation of fluid inclusions [29].

3.2. U–Pb

U–Pb ages for zircons from four samples were determined using a CAMECA ims 1270 ion microprobe (Table 2). Zircon grains were mounted in epoxy, polished, and coated with ~100 Å of Au. Operating conditions for the ion microprobe are described in [27], including oxygen flooding to a pressure of $\sim 4 \times 10^{-5}$ to increase Pb^+ yields. U–Pb ages were determined by comparison with standard zircon AS-3 [30]. Initial analyses of ANG1-11400 utilized a ~12 nA primary O^- beam focused to a $\sim 25 \times 35$

Table 2
Zircon U–Pb ion microprobe results

Sample	Intercept age [a] (Ma)	$^{207}Pb/^{206}Pb$ [b]	MSWD
ANG1-11400	1.13 ± 0.04	0.91 ± 0.09	1.1
FF52-9040	1.18 ± 0.02	0.81 ± 0.03	4.5
LF23-9800	1.25 ± 0.04	0.82 ± 0.01	7.1
LF23-9540	1.24 ± 0.03	0.81 ± 0.03	4.5

[a] Calculated from intercept of regression line with concordia on the $^{207}Pb/^{206}Pb$ vs. $^{238}U/^{206}Pb$ diagram. Errors are 1σ.
[b] Common $^{207}Pb/^{206}Pb$ calculated from *y*-intercept on the $^{207}Pb/^{206}Pb$ vs. $^{238}U/^{206}Pb$ diagram. Errors are 1σ.

μm spot with subsequent measurements using a 30 nA beam. The higher beam currents offered mixed benefits as Pb yields were increased while the stability of the calibration curve was degraded from the typical ±2% [27] to ±5%.

4. Results

4.1. U–Pb zircon ages

An important benefit of using the ion microprobe to analyze zircons is the ability to resolve and avoid inherited radiogenic Pb. The simplest approach for determining U–Pb ages for young zircons is to calculate $^{206}Pb/^{238}U$ ages assuming a modern common $^{206}Pb/^{204}Pb$ ratio of 18 [31] and using ^{204}Pb as the basis to estimate common lead. Ages calculated in this manner reveal that 4 of the 73 zircons measured from the 4 samples (ages of 2.1, 2.3, 8.0, and 78 Ma) are likely restitic and unrelated to the crystallization age of the GPC. Relatively imprecise $^{206}Pb/^{238}U$ model ages calculated for the remaining 69 grains define a normal distribution between 0.6 and 1.5 Ma with a weighted mean of 1.18 ± 0.03 Ma and an MSWD of 2.4. The low Pb concentrations of these young zircons result in calculated $^{206}Pb/^{238}U$ ages that are highly sensitive to the magnitude of the common lead correction, so we also analyzed our results using an isochron approach. If the grains have concordant U–Pb systems, a good assumption given their youth and low U contents (typically 200–700 ppm), the U–Pb data uncorrected for common lead should define a mixing array between common and radiogenic components on a $^{207}Pb/^{206}Pb$ vs.

^{238}U/^{206}Pb concordia plot [32]. The intercept of this array with the ^{207}Pb/^{206}Pb axis yields the common Pb composition while the intersection with concordia gives the age of crystallization [33]. Treatment of the data using a conventional concordia diagram yielded similar results, as expected.

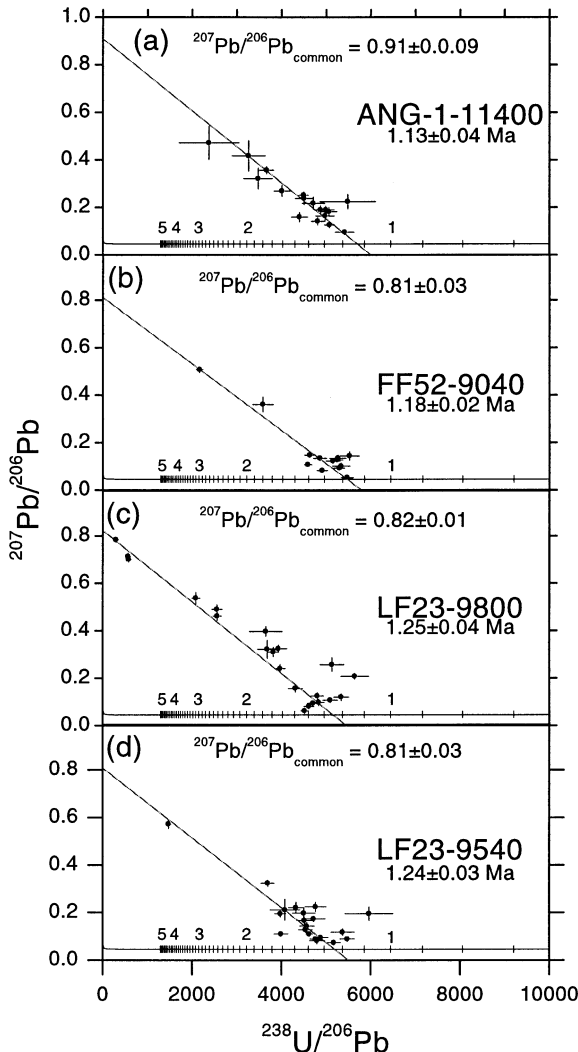U–Pb concordia ages for each of the four sam-

Fig. 2. ^{207}Pb/^{206}Pb vs. ^{238}U/^{206}Pb concordia diagrams [32] for U–Pb ion microprobe results for zircons from four samples of granite from the GPC. Error bars are $\pm 1\sigma$. U–Pb ages are from intersection of best-fit [34] line (isochron) with concordia [33]. Common Pb is indicated by the intercept of the isochron with the ^{207}Pb/^{206}Pb axis.

ples (Fig. 2; Table 2) vary between 1.13 ± 0.04 and 1.25 ± 0.04 Ma, in agreement with the weighted mean of the model ages. The uncertainties reflect correlation between ^{206}Pb/^{238}U and ^{207}Pb/^{235}U [34]. The MSWD values are high because the point-to-point reproducibility of the standard data used to define the UO$^+$/U$^+$ vs. Pb$^+$/U$^+$ calibration curve is not completely accounted for in propagating the error associated with the Pb/U relative sensitivity factor. To correct for this effect we have multiplied the initial uncertainties by the square root of the MSWD. Doing so yields uncertainties comparable to those anticipated from the reproducibility of the calibration curve (e.g., 0.06 m.y. or 5%). Reproducibility of results from a single sample appears to be better than 5%. In addition, ion microprobe measurements performed for the same grains of ANG1-11400 using a different instrument (Stanford-USGS SHRIMP RG) yield a result similar to ours (1.11 ± 0.06 Ma, common ^{207}Pb/^{206}Pb $= 0.80 \pm 0.06$, MSWD = 0.60; C.R. Bacon, pers. commun., 1999). Moreover, the observation that results from closely spaced, and presumably genetically related samples (well LF-23 in Table 2) are statistically indistinguishable, indicates that intersample reproducibility is also better than 5%. Finally, most samples yield similar common ^{207}Pb/^{206}Pb values that are comparable with modern and anthropogenic ratios [31].

Our U–Pb age analysis assumes initial equilibrium in intermediate daughter products. While equilibrium ^{234}U activity may reasonably be assumed for zircon, initial deficit in ^{230}Th is likely and results in calculated ages that are too young [35,36]. The maximum effect is 0.13 m.y. or roughly 10% of our calculated values if initial abundances of Th were negligible [35]. Since the zircons contain small amounts of Th, the ensuing error is lower and likely within our stated uncertainties.

4.2. ^{40}Ar/^{39}Ar step-heating results

Biotite age spectra from two samples (Table 1) yield ~1.1 Ma terminal ages. Essentially all K-feldspars examined yield resolvable age gradients. While the thermochronologic implications of the ^{40}Ar/^{39}Ar data are considered in the following section, we point out that half of the K-feldspars analyzed yield high-temperature 'terminal ages' that overlap

U–Pb ages from coexisting zircon within uncertainty (Tables 1 and 2). Moreover, virtually all K-feldspar terminal ages are within 0.2 Ma of the youngest zircon result.

4.3. Feldspar thermal history modeling

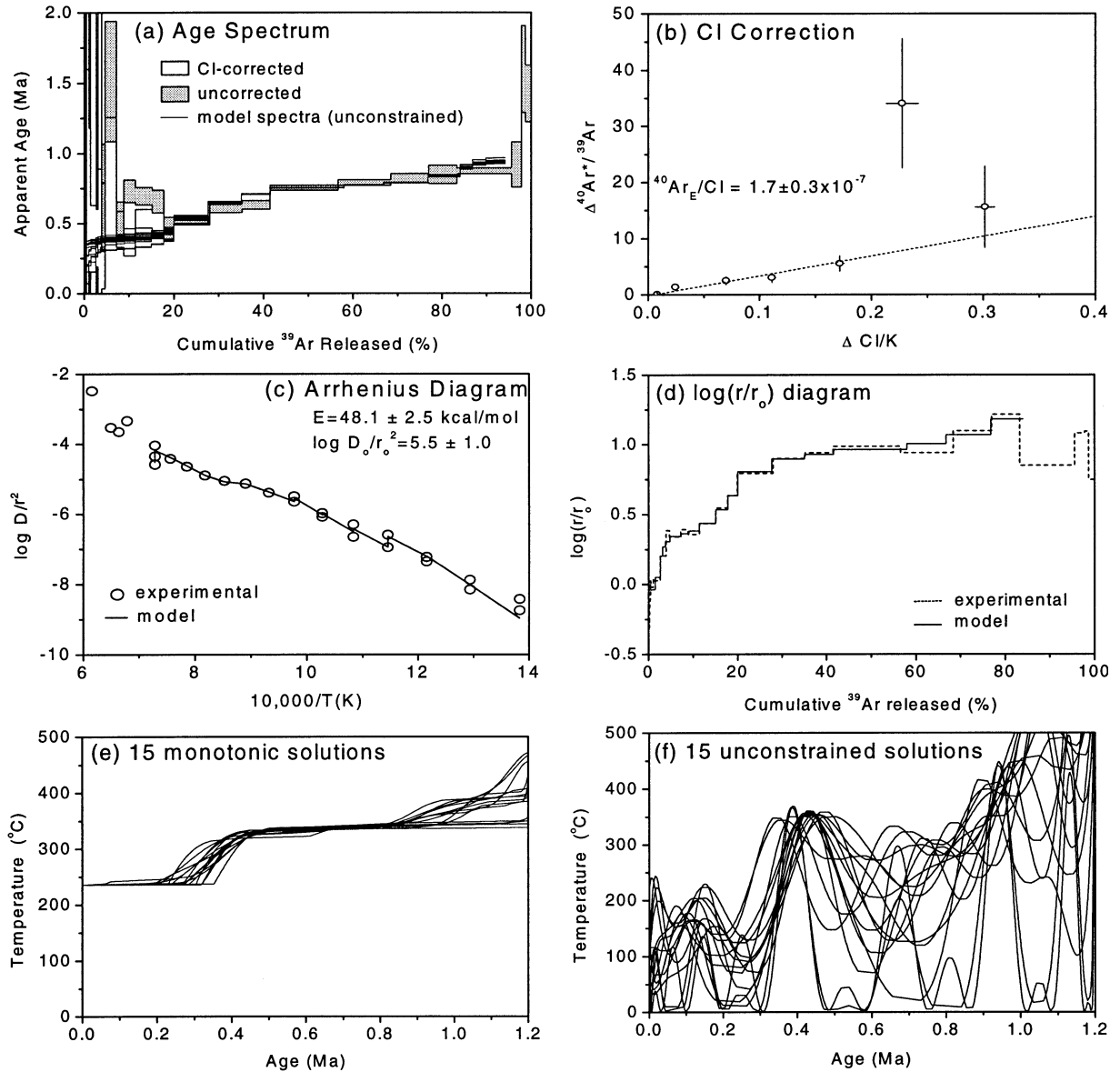Thermal history modeling of the K-feldspar ^{40}Ar/^{39}Ar age spectra to determine possible and probable

Fig. 3. Analytical data and modeling results for K-feldspar from GDC5-7800. (a) Measured age spectrum, age spectrum corrected for ^{40}Ar$_E$, and age spectra from 15 unconstrained model results. (b) Results of low-temperature isothermal duplicates [29] showing correlation of ^{40}Ar$_E$ with Cl and resulting correction (dashed line). (c) Arrhenius diagram showing measured and modeled diffusion values calculated from ^{39}Ar release. (d) Measured and modeled log (r/r_0) plots. (e) Fifteen representative monotonic thermal histories that reproduce the Cl-corrected age spectrum. Final temperature restricted to 235ºC to correspond to present conditions. (f) Fifteen unconstrained thermal histories that reproduce Cl-corrected age spectrum.

temperature–time (T–t) paths was performed on five samples (Table 1) by applying the MDD model [19]. Details of the computational approach are given in [27–29]. The outcome of the modeling is illustrated with the results from sample GDC5-7800 (Fig. 3). Least-squares regression [34] of $\Delta^{40}Ar^*/^{39}Ar$ and $\Delta Cl/K$ values determined from successive isothermal heating steps (Fig. 3b) yields the $^{40}Ar_E/Cl$ value required to correct model ages in Fig. 3a for fluid inclusion-hosted $^{40}Ar_E$ [29]. Least-squares fitting of Arrhenius data calculated from ^{39}Ar release (Fig. 3c,d) yield MDD parameters that characterize the laboratory Ar diffusion properties of the sample [27]. Because domain distributions capable of reproducing the measured Arrhenius data are non-unique [28], we propagate the ensuing uncertainty by using five equivalent MDD parameter sets for each sample in the thermal history analysis.

If laboratory-determined K-feldspar Ar diffusion properties adequately mimic those in nature, the step-heating results provide the basis for recovering sample thermal histories. Correlated behavior of the age and ($\log r/r_0$) spectra (Fig. 3a,d) indicate that this fundamental assumption is valid. In the present study, we apply the approach of [28,29] to obtain sets of post-crystallization thermal histories that best fit the Cl-corrected age spectrum by either constraining temperature to decline monotonically (Fig. 3e) or vary freely (Fig. 3f). Note that we have restricted monotonic solutions to temperatures in excess of the ambient value of 235°C [1].

Monotonic cooling solutions calculated from equivalent domain distributions (Fig. 3e) generally describe similar temperature–time (T–t) paths over the temperature interval corresponding to partial Ar retention (i.e. 350–150°C). Given this concordance, it is useful to represent the results by calculating 90% confidence intervals [29] for both the mean and the overall distribution of successful solutions (Fig. 4). In contrast, unconstrained T–t solutions vary widely (Fig. 3f). To best represent thermal history constraints afforded by the latter, we calculate the density of the unconstrained successful solutions in T–t space (Fig. 5). In order to minimize bias related to initial conditions and the number of successful solutions obtained, we subtract the input (trial) thermal histories and normalize the result by the total number of successful solutions [28]. The
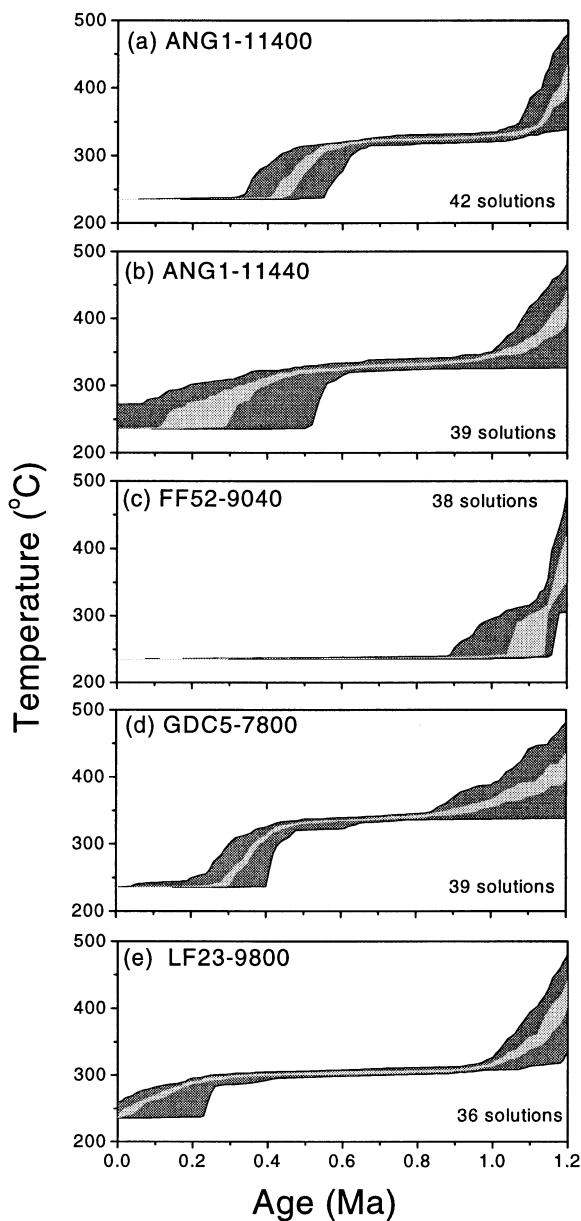

Fig. 4. Best-fit monotonic thermal histories for K-feldspars from the Geysers samples. The 90% confidence intervals for the mean values and overall distributions are shown by light and dark shading, respectively.

utility of this approach is that regions of T–t space where the thermal history is tightly constrained are readily revealed. Moreover, because T–t space above the region traversed by the unconstrained solutions
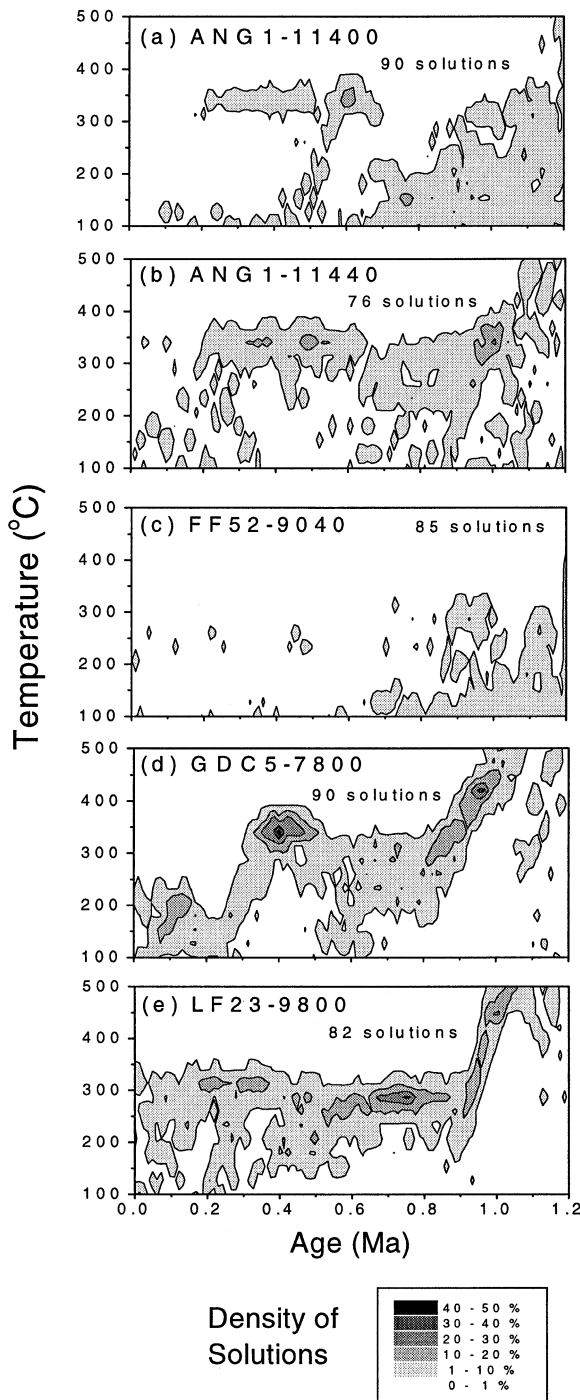
Fig. 5. Contours of best-fit unconstrained thermal histories for K-feldspars from the Geysers samples. The densities have been converted to percentages to allow for the different numbers of solutions for each sample.

is strictly forbidden, the results also constrain the maximum temperature at all times subsequent to the oldest ages recorded.

Near concordance of the zircon and K-feldspar terminal ages, which are based on the large diffusion domains, require all samples to cool below 350°C by 0.9 Ma. Thereafter, monotonic cooling history results from FF52-9040 differ substantially from the other samples (Fig. 4). Cooling to 235°C by 0.90 Ma (Fig. 4c) is required to account for the 1.20±0.01 Ma ages yielded by FF52-9040 K-feldspar over the final 60% of ^{39}Ar release (Table 1). Monotonic cooling solutions for the remaining four K-feldspars require nearly isothermal conditions of 300–350°C between ~1.0 and 0.4–0.2 Ma. Of these samples LF23-9800 indicates the lowest temperatures (~300°C; Fig. 4e) while GDC5-7800 requires the highest (~350°C; Fig. 4d).

Unconstrained solutions clearly demonstrate that post-crystallization reheating at times more recent than 0.9 Ma could have been significant for all samples except FF52-9040 (Fig. 5c). The possibility of post-crystallization reheating is most apparent for GDC5-7800, which indicates a high probability that the sample experienced ~340°C at 0.4 Ma (Fig. 5d). While less distinctive, results from ANG1-11400 (Fig. 5a) and ANG1-11440 (Fig. 5b) also suggest reheating to ~340°C at 0.6–0.4 Ma. Sample LF23-9800 (Fig. 5e) also appears to preclude simple post-crystallization cooling but indicates somewhat lower temperatures (~250–300°C) for the interval 0.9–0.2 Ma.

5. Discussion

5.1. Emplacement and cooling of the Geysers plutonic complex

We interpret the U–Pb zircon ages as indicating that the granite crystallized at 1.18 ± 0.03 Ma. Although ion microprobe analysis has allowed us to identify and avoid inherited radiogenic Pb derived from restitic grains, it is likely that the zircon we have analyzed contained below equilibrium values of initial ^{230}Th in zircon [36]. Hence the actual crystallization age could exceed our estimate by as much as 0.13 Ma [35]. Alternatively, zircons could have

crystallized somewhat earlier than solidus conditions were reached. Pre-eruptive residence of early-crystallized zircon on time scales important to our study (~0.3 Ma) has been documented in silicic magma chambers [37]. Despite these uncertainties, the internal consistency of the U–Pb age results (Fig. 2; Table 2), their close correspondence with the terminal ^{40}Ar/^{39}Ar ages from coexisting K-feldspar (Table 1), the shallow level of emplacement [1], and their agreement with independently determined ^{40}Ar/^{39}Ar ages from the likely volcanic equivalent, the 1.19 ± 0.01 Ma Alder Creek rhyolite [11], all seem to require that the duration of pre-eruptive residence for these zircons was <0.1 m.y. While crystallization ages for the granite and microgranite are not directly constrained by our results, independent constraints [12] suggest that the entire GPC may have been emplaced within the short (0.1 m.y.) time interval [3,11] represented by the overlying Cobb Mountain volcanic center (Fig. 1).

The rapid cooling to <350ºC by 0.9 Ma indicated by our K-feldspar thermal histories is consistent with the shallow level of emplacement [1]. Most K-feldspar thermochronometric results require that high temperatures of ~300–350ºC were maintained at 2.5–3.5 km depths over the 0.7 m.y. interval following intrusion (Fig. 4) or that episodic reheating to 350ºC took place at 0.6–0.4 Ma (Fig. 5). Only K-feldspar from FF52-9040 appears to have experienced a relatively simple post-crystallization cooling history and this may result from its location along the southwest margin of the GPC, the steam reservoir, and the heat flow anomaly (Fig. 1). In this setting more rapid initial cooling and minimal effects of subsequent thermal events might be expected. Likewise, K-feldspar results from LF23-9800 may also differ from the remaining samples because of proximity to the northeast margin of the GPC, to the later heat source(s), or both. While samples from ANG1 also reside along the northeast margin they originate from somewhat greater depths where the boundaries of the GPC are not well known (Fig. 1).

5.2. Timing of the onset of vapor-dominated conditions

The mechanism(s) responsible for establishing vapor-dominated conditions within the Geysers geothermal field remain poorly understood. Theoretical models suggest that the transformation resulted from rapid fluid venting or boil-off and that temperature was precipitously reduced throughout affected portions of the system [38]. Study of the evolution of trapped fluids within the complex has allowed characterization of the temperatures that prevailed at the time the transformation occurred [1]. These fluid inclusion data indicate that conditions were ~265ºC in the central field and ~290ºC in the northern field. Previous monotonic cooling MDD thermal history results from hydrothermal adularia from the northwestern Geysers indicate rapid cooling from >300ºC to <260ºC from 0.28 to 0.25 Ma and imply that the steam-dominated reservoir in this portion of the field formed roughly at 0.26 Ma [12]. With the exception of sample FF52, monotonic and unconstrained thermal history solutions obtained for all of our samples from the central field record a broadly similar timing for rapid cooling through 265ºC (Figs. 4 and 5). The observed variability likely reflects both difficulty in adequately resolving ^{40}Ar/^{39}Ar age from the low-temperature gas release and differences in sample position.

5.3. Heat flow considerations

Heat flow calculations for shallow plutons similar in dimension to the GPC indicate that less than 0.3 m.y. should be required for their upper regions to cool below 250ºC [15]. Although results in Figs. 4 and 5 indicate that cooling below 350ºC occurred within 0.2 m.y. of crystallization, only FF52-9040 K-feldspar cooled to below 250ºC by 0.9 Ma. Both maintenance of 300–350ºC conditions after 0.9–0.4 Ma (Fig. 4) or reheating at 0.6–0.4 Ma (Fig. 5) is difficult to explain without invoking additional heat sources. Moreover, an extensive heat source in the subsurface of the Geysers–Clear Lake region is required by present-day heat flow measurements [6]. Below we describe conductive heat flow calculations involving additional intrusive heat sources to test if the addition of such sources subsequent to intrusion of the GPC might account for the thermal histories results. The GPC is represented with a single 4 km diameter pluton that was instantaneously emplaced at 1.2 Ma 3 km beneath the surface at the left margin of the regional heat flow anomaly (Figs. 1 and 6).
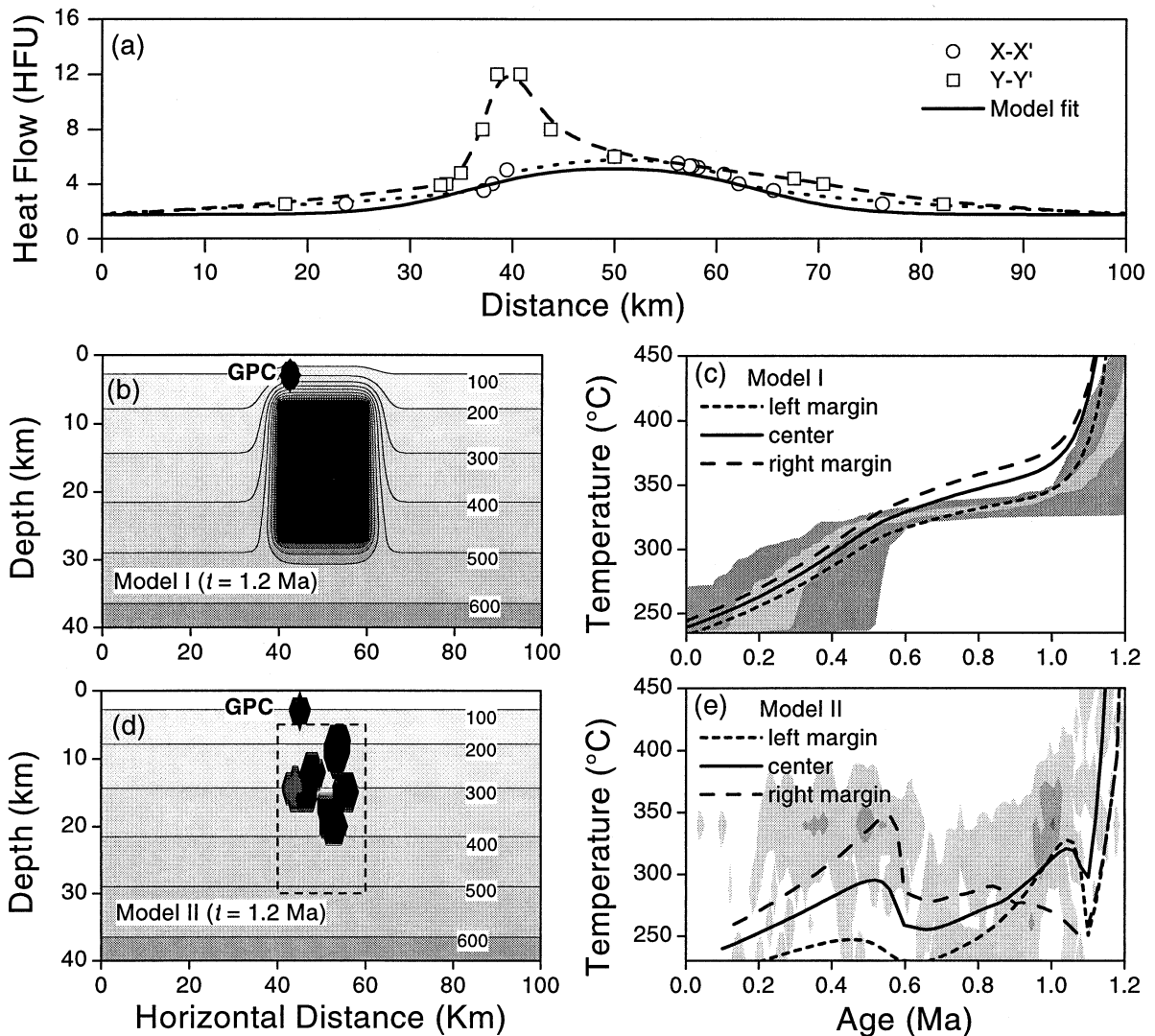
Fig. 6. Results of heat flow modeling to explain the thermal history constraints of the Geysers geothermal field. (a) Surface heat flow profiles across the CLVF. Approximate locations of sections are given in Fig. 1b. (b) A large, convecting intrusive body emplaced at 1.2 Ma below the GPC (small body at 3 km depth). Shaded bands represent background geothermal gradient with temperatures in °C. (c) Thermal histories for the center and margins of the GPC predicted by Model I. MDD monotonic cooling results for ANG1-11400 shown for comparison. (d) Multiple intrusions emplaced randomly at intervals of 0.1 m.y. between 1.1 and 0.6 Ma below the GPC. (e) Thermal histories for the center and margins of the GPC predicted by Model II. MDD unconstrained cooling results for ANG1-11440 shown for comparison.

Calculations were performed using a 2-D Crank–Nicholson finite-difference algorithm [39]. Parameterization of the models is outlined in Fig. 6. Because conductive thermal models are inadequate to describe heat transfer within the steam field, we focus primarily upon the earlier subsolidus history (>0.4 Ma). A conceptual model for late-stage development involving steam-mediated heat advection has been developed by [40].

5.3.1. Long-lived magma chamber (Model I)

We test the hypothesis of a single convecting magma chamber [16,18] by placing a 20 km wide by 20 km deep body 7 km beneath the surface at 1.2

Ma. Extrapolation of results from [38] indicate that temperature-dependent viscosity and heat loss into adjacent country rocks likely limit vigorous convection within such a body to ca. 0.6 m.y. Accordingly, we reduce temperature in the magma chamber linearly from 1000ºC to 700ºC during the convective phase (1.2–0.6 Ma) and by conduction thereafter.

5.3.2. Episodic intrusion (Model II)

We investigate the aggregate effect of smaller bodies [17] by episodically intruding random distributions of 2–4 km diameter plutons into the same region that was occupied by the single magma chamber in *Model I* in successive 0.1 m.y. intervals between 1.2 and 0.6 Ma. The thermal effects of intrusion are simulated by setting the temperature of grid points contained within pluton boundaries to solidus values (850–1000ºC) at the time of emplacement and by allowing the affected region to cool by conduction following each intrusive pulse.

5.3.3. Model constraints and results

In both models, parameters were varied to reproduce the thermal history results (Figs. 4 and 5) and observed present-day heat flow (Figs. 1 and 6a). We assume that profile X–X′ is most representative of the regional feature while Y–Y′ is significantly influenced by the Geysers steam field. As discussed below, both models are capable of reproducing observed thermal histories and heat flow values along X–X′ (Fig. 6a). Neither of the conductive models, however, is capable of matching Y–Y′ while still satisfying the K-feldspar thermal history constraints. It seems probable that the high-amplitude anomaly in Y–Y′ results from steam-mediated, heat advection that, until recently, maintained near uniform 35 bar, 240ºC conditions [1] throughout much of the steam field [40].

Results from *Model I* (Fig. 6b) are best compared to the monotonic cooling results (Fig. 4). The three predicted T–t histories in Fig. 6c correspond to the left, center, and right margins of the GPC. Over the first 0.1 m.y., predicted thermal histories reflect the rapid cooling characteristic of shallow plutonic bodies. With continued evolution, however, temperatures are maintained by the magma chamber, which affects the left margin less than the right. The lateral thermal gradient developed between these two model posi-

tions (ca. 50ºC) is comparable to that indicated for the GPC from 1.0 to 0.4 Ma (compare Fig. 4c with Fig. 4e). Although rapid cooling at ∼0.4 Ma is not predicted by this model, advective heat transfer accompanying catastrophic fluid expulsion as proposed by [40] could account for the K-feldspar thermal history results [12].

The results for repeated intrusion (Model II) in Fig. 6d are best compared to the episodic heating models shown in Fig. 5. While the region, on average, is maintained at elevated T, large variation in T–t histories for samples positioned at similar depths is expected. For example, results for one particular random sequence of intrusions cause much larger lateral thermal gradients in the shallow pluton than are observed in Model I (compare Fig. 6c with Fig. 6e). As a result it is probable that regionally distributed sampling of K-feldspar would reveal a heterogeneous age pattern with many samples being completely reset at varying times. Our 10 km lateral sampling across the axial trend of the geothermal field (Fig. 1) apparently supports significant reheating only at ∼0.6–0.4 Ma (Fig. 5), coincident with the largest pulse of silicic volcanism in the CLVF [2]. Similarly, geochemical [1] and thermochronologic [12] evidence for recent intrusion in the northwest steam field suggest a ca. 0.6 m.y. event.

6. Conclusions

Our new U–Pb zircon and ^{40}Ar/^{39}Ar K-feldspar thermochronologic results together with those of previous studies [3,11,12] allows us to conclude the following.

(1) The granite and probably the microgranite crystallized at 1.18 ± 0.03 Ma and the entire GPC was likely emplaced within ∼0.1 m.y.

(2) The temperature of the system at the sampled depths dropped rapidly to less than 350ºC by 0.9–1.0 Ma. Thereafter, either near-isothermal conditions maintained between 350º and 300ºC or there was reheating to ∼350ºC about 0.6–0.4 Ma.

(3) Our results support the previous conclusion [12] that vapor-dominated conditions within the geothermal system were established ∼0.26 Ma.

(4) Conductive heat flow calculations indicate that a heat source, in addition to the intrusive mass of the

GPC, is required to account for the observed thermal evolution of the complex. Our K-feldspar T–t results may be adequately explained by either a large, long-lived magma chamber [16,18] or massive intrusion of smaller plutons [17]. We intend to perform additional U–Pb and ^{40}Ar/^{39}Ar work with a wider distribution of samples within the GPC so that thermal models of the Geysers geothermal system can be refined.

Acknowledgements

References

[1] J.N. Moore, R.P. Gunderson, Fluid inclusion and isotopic systematics of an evolving magmatic-hydrothermal system, Geochim. Cosmochim. Acta 19 (1995) 3887–3907.

[2] J.M. Donnelly-Nolan, B.C. Hearn Jr., G.H. Curtis, R.E. Drake, Geochronology and evolution of the Clear Lake Volcanics, in: R.J. McLaughlin, J.M. Donally-Nolan (Eds.), Research in the Geysers–Clear Lake Geothermal Area, Northern California, U.S. Geol. Surv., Prof. Pap. 1141 (1981) 47–60.

[3] B.C. Hearn Jr., J.M. Donnelly-Nolan, F.E. Goff, Geologic map and structure sections of the Clear Lake volcanics, northern California, USGS Misc. Invest. Map I-2362, 1995.

[4] K.F. Fox Jr., R.J. Fleck Curt, G.H. Curtis, C.E. Meyer, Implications of the northwestwardly younger age of the volcanic rocks of west-central California, Geol. Soc. Am. Bull. 96 (1985) 647–654.

[5] K.H. Williamson, Development of a reservoir model for The Geysers geothermal field, in: C. Stone (Ed.), Monograph on the Geysers Geothermal Field, Geotherm. Res. Council Spec. Rep. 17 (1992) 179–188.

[6] M. Walters, J. Coombs, Heat flow regime in the Geysers–Clear Lake area of northern California, Geotherm. Res. Council Trans. 13 (1989) 491–502.

[7] A. Schriener, G.A. Suemnicht, Subsurface intrusive rocks at the Geysers geothermal area, California, in: M.L. Silberman, C.V. Field, A. Berry (Eds.), Proceedings of the Symposium on Mineral Deposits of the Pacific Northwest, Corvallis, OR, 1980, U.S. Geol. Surv. Open-File Rep. 81-355 (1981) 295–302.

[8] R.C. Thompson, Structural stratigraphy and intrusive rocks at the Geysers geothermal field, Geotherm. Res. Council. Trans. 13 (1989) 481–485.

[9] J.B. Hulen, D.L. Nielson, The Geysers felsite, Geotherm. Res. Council Trans. 20 (1996) 295–306.

[10] J.M. Donnelly-Nolan, M.G. Burns, F.E. Goff, E.K. Peters, J.M. Thompson, The Geysers–Clear Lake area, California: thermal waters, mineralization, volcanism, and geothermal potential, Econ. Geol. 88 (1993) 301–316.

[11] B.D. Turrin, J.M. Donnelly-Nolan, B.C. Hearn Jr, ^{40}Ar/^{39}Ar ages from the rhyolite of Alder Creek, California: age of the Cobb Mountain normal polarity subchron revisited, Geology 22 (1994) 251–254.

[12] J.B. Hulen, M.T. Heizler, J.A. Stimac, J.N. Moore, J.C. Quick, New constraints on the timing of magmatism, volcanism, and the onset of vapor-dominated conditions at the Geysers steam field, California, in: Proc. 22nd Workshop on Geothermal Reservoir Engineering, Stanford University, Stanford, CA, 1997, pp. 75–81.

[13] F.S. Pulka, Subsurface Geology at Ford Flat, Geysers Geothermal Field, Northern California, M.S. Thesis, Michigan Technological University, Houghton, MI, 1991, 324 pp.

[14] G.B. Dalrymple, Preliminary report on ^{40}Ar/^{39}Ar incremental heating experiments on feldspar samples from the felsite unit, Geysers geothermal field, California, U.S. Geol. Surv. Open-File Rep. 92-407 (1992) 15 pp.

[15] D. Norton, J. Knight, Transport phenomena in hydrothermal systems: cooling plutons, Am. J. Sci. 277 (1977) 937–981.

[16] W.F. Isherwood, Geophysical overview of the Geysers, in: R.J. McLaughlin, J.M. Donnelly-Nolan (Eds.), Research in the Geysers–Clear Lake Geothermal Area, Northern California, U.S. Geol. Surv., Prof. Pap. 1141 (1981) 83–95.

[17] W.D. Stanley, H.M. Benz, M.A. Walters, A. Villasenor, B.D. Rodriquez, Tectonic controls on magmatism in the Geysers–Clear Lake region: evidence from new geophysical models, Geol. Soc. Am. Bull. 100 (1998) 1193–1207.

[18] R.J. McLaughlin, Tectonic setting of pre-Tertiary rocks and its relation to geothermal resources in the Geysers–Clear Lake area, in: R.J. McLaughlin, J.M. Donnelly-Nolan (Eds.), Research in the Geysers–Clear Lake Geothermal Area, Northern California, U.S. Geol. Surv. Prof. Pap. 1141 (1981) 3–23.

[19] O.M. Lovera, F.M. Richter, T.M. Harrison, ^{40}Ar/^{39}Ar thermochronometry for slowly cooled samples having a distribution of diffusion domain sizes, J. Geophys. Res. 94 (1989) 17917–17935.

[20] W.R. Dickinson, W.S. Snyder, Geometry of triple junctions related to the San Andreas transform, J. Geophys. Res. 84 (1979) 561–572.

[21] A.H. Lachenbruch, J.H. Sass, Heat flow and energetics of the San Andreas fault zone, J. Geophys. Res. 85 (1980) 6185–6222.

[22] K.P. Furlong, W.D. Hugo, G. Zandt, Geometry and evolu-

tion of the San Andreas fault zone in northern California, J. Geophys. Res. 94 (1989) 3100–3110.

[23] H.M. Benz, G. Zandt, D.H. Oppenheimer, Lithospheric structure of northern California from teleseismic images of the upper mantle, J. Geophys. Res. 97 (1986) 4791–4807.

[24] J.A. Stimac, Evolution of the Silicic Magmatic System at Clear Lake, California, from 0.6 to 0.3 Ma, Ph.D. Dissertation, Queens University, Kingston, ON, 1991, 399 pp.

[25] D.H. Oppenheimer, Extensional tectonics at the Geysers geothermal area, California, J. Geophys. Res. 91 (1986) 11436–11476.

[26] G.B. Dalrymple, E.C. Alexander Jr., M.A. Lanphere, G.P. Kraker, Irradiation of samples for ^{40}Ar/^{39}Ar dating using the Geological Survey TRIGA reactor, U.S. Geol. Surv. Prof. Pap. 1176 (1981) 55 pp.

[27] X. Quidelleur, M. Grove, O.M. Lovera, T.M. Harrison, A. Yin, F.J. Ryerson, The thermal evolution and slip history of the Renbu Zedong Thrust, southeastern Tibet, J. Geophys. Res. 102 (1997) 2659–2679.

[28] O.M. Lovera, M. Grove, T.M. Harrison, K.I. Mahon, Systematic analysis of K-feldspar ^{40}Ar/^{39}Ar step heating results, I, Significance of activation energy determinations, Geochim. Cosmochim. Acta 61 (1997) 3171–3192.

[29] T.M. Harrison, M.T. Heizler, O.M. Lovera, C. Wenji, M. Grove, A chlorine disinfectant for excess argon released from K-feldspar during step-heating, Earth Planet. Sci. Lett. 123 (1994) 95–104.

[30] J.B. Paces, J.D. Miller, Precise U–Pb age of Duluth Complex and related mafic intrusions, northeastern Minnesota: geochronological insights into physical, petrogenetic, paleomagnetic, and tectonomagmatic processes associated with the 1.1 Ga midcontinent rift system, J. Geophys. Res. 98 (1993) 13997–14013.

[31] G. Faure, Principles of Isotope Geology (2nd ed.), Wiley, New York, 1986, 589 pp.

[32] F. Tera, G.J. Wasserburg, U–Th–Pb systematics on lunar rocks and inferences about lunar evolution and the age of the moon, Proc. 5th Lunar Conf., Geochim. Cosmochim. Acta 2 (Suppl. 5) (1974) 1571–1599.

[33] S.L. Baldwin, T.R. Ireland, A tale of 2 eras: Pliocene–Pleistocene unroofing of Cenozoic and late Archean zircon from active metamorphic core complexes, Solomon Sea, Papua New Guinea, Geology 23 (1995) 1023–1026.

[34] K. Mahon, The New 'York' regression: application of an improved statistical method to geochemistry, Int. Geol. Rev. 38 (1996) 293–303.

[35] K.R. Ludwig, Effect of initial radioactive–daughter product disequilibrium on U–Pb isotope apparent ages of young minerals, U.S. Geol. Surv. J. Res. 5 (1977) 663–667.

[36] U. Schärer, The effect of initial ^{230}Th on young U–Pb ages: the Makalu case, Himalaya, Earth Planet. Sci. Lett. 67 (1984) 191–204.

[37] M.R. Reid, C.D. Coath, T.M. Harrison, K.D. McKeegan, Prolonged residence times for the youngest rhyolites associated with Long Valley Caldera: ^{230}Th/^{238}U ion microprobe dating of young zircons, Earth Planet. Sci. Lett. 150 (1997) 27–39.

[38] M. Shook, Development of a vapor-dominated reservoir with a 'high-temperature' component, Geothermics 24 (1995) 489–505.

[39] W.H. Press, B.P. Flannery, S.A. Teukolsky, W.T. Vetterling, Numerical Recipes: The Art of Scientific Computing, Cambridge University Press, Cambridge, 1986, 818 pp.

[40] J.T. Ratcliff, G. Schubert, B. Carrigan, B. Travis, G. Valentine, Effects of temperature-dependent viscosity and wall-rock conduction on thermal convection in magma reservoirs, J. Geophys. Res. (in press).

[41] J.R. Taylor, An Introduction to Error Analysis, University Science books, Mill Valley, CA, 1982, 270 pp.